

# Direct reduction of synthetic rutile using the FFC process to produce low-cost novel titanium alloys

L. L. Benson<sup>1</sup> · I. Mellor<sup>2</sup> · M. Jackson<sup>1</sup>

Received: 9 November 2015 / Accepted: 31 December 2015 / Published online: 22 January 2016  
© The Author(s) 2016. This article is published with open access at Springerlink.com

**Abstract** Typically, pure TiO<sub>2</sub> in pellet form has been utilised as the feedstock for the production of titanium metal via the solid state extraction FFC process. For the first time, this paper reports the use of loose synthetic rutile powder as the feedstock, along with its full characterisation at each stage of the reduction. The kinetics and mechanism of the reduction of synthetic rutile to a low oxygen titanium alloy have been studied in detail using a combination of X-ray diffraction, scanning electron microscopy, oxygen analysis, and X-ray fluorescence techniques. Partial reductions of synthetic rutile enabled a reaction pathway to be determined, with full reduction to a low oxygen titanium alloy occurring at 16 h. Major remnant elements from the Becher process within the feedstock were followed throughout the process, with a particular emphasis placed on the reduction behaviour of iron within the alloy. Although impurities such as Fe, Al, and Mn are found in the feedstock and alloy, no major deviations from previously reported reaction mechanisms and phase transformations utilising a pure porous (25–30 % porosity) TiO<sub>2</sub> precursor were found. Following reduction, the titanium alloy powder produced from synthetic rutile (approx. 3500 ppm oxygen) has been consolidated via an emerging rapid sintering technique, and its microstructure analysed. This work will act as the baseline for future alloy development projects aimed at producing low-cost titanium alloys directly from synthetic rutile. Producing titanium

alloys directly from synthetic rutile may negate the use of master alloy additions to Ti in the future.

## Introduction

Since its publication in 2000 [1], the FFC process, named after its inventors, Fray, Farthing and Chen, has generated a substantial amount of interest. Alongside significant academic research [2–13], a spin-off technology company, Metalysis was established to capitalise upon the new technology. Facilitating the extraction of metals from their ores and/or oxides, this process has the potential to drastically reduce the cost of the production of metals, particularly titanium. Titanium alloys are renowned for their superior properties—excellent biocompatibility, superb corrosion resistance, and a high strength to weight ratio. However, due to the expense of both extraction and fabrication, titanium alloys are also well known for their relatively high cost, achieving a status as a somewhat premium metal, despite the abundance of rutile and ilmenite ores. Hence, application of the FFC Metalysis process to produce titanium alloy powders, in conjunction with more economical downstream consolidation techniques, could lead to a step-change in the economics of titanium, allowing an affordable, streamlined production route of titanium metal components. Sectors outside of the aerospace industry are set to reap the largest reward, with the production of low-cost titanium being hailed as a long-term Holy Grail, particularly in the automotive industry [14].

Due to its commercially rewarding nature, a considerable amount of research has been undertaken to further develop the process. Much research has focused on taking advantage of its solid state extraction; by avoiding melting procedures, alloys previously prone to segregation effects

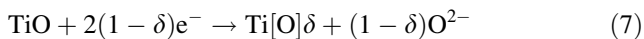
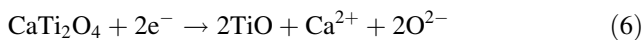
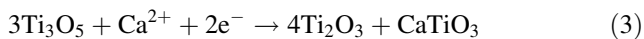
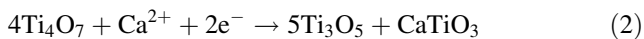
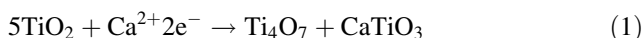
✉ L. L. Benson  
LLbenson1@shef.ac.uk

<sup>1</sup> Department of Materials Science and Engineering,  
The University of Sheffield, Sheffield S1 3JD, UK

<sup>2</sup> Metalysis Ltd, Unit 2 - Farfield Park, Manvers Way,  
Wath-Upon-Deerne, Rotherham S63 5DB, UK

can be produced in a much more cost-efficient manner [8, 10]. Other research has focused on understanding the reaction pathway and kinetics of the process, facilitating the optimisation of the procedure [2–5, 15].

A typical Metalysis FFC cell consists of a graphite anode and a cathode—usually the metal oxide, immersed in a bath of molten  $\text{CaCl}_2$  [1]. Once a current is applied in an inert atmosphere at elevated temperatures, oxygen is ionised and diffuses through the electrolyte to the anode, releasing carbon oxides, CO and  $\text{CO}_2$  [2]. A detailed reaction mechanism published in 2005 by Schwandt et al. [2] has led to both a deeper understanding of reaction pathway, as well as improvements in the efficiency of the process in further work [4]. Equations 1–7 outline the overall reaction mechanism.



On the initial application of the current, it is understood that  $\text{Ca}^{2+}$  ions are first incorporated into the cathode from the electrolyte, producing calcium titanate,  $\text{CaTiO}_3$ . Suboxides of titanium are sequentially formed, in order of decreasing oxygen content to reach  $\text{Ti}_2\text{O}_3$ . It is accepted in the field that the higher ordered Magnéli phases ( $\text{Ti}_x\text{O}_{2x-1}$ , where  $4 \leq x \leq 9$ ) are likely to have formed prior to the formation of  $\text{Ti}_4\text{O}_7$  [3]. Suboxide TiO is eventually formed which combines with  $\text{CaTiO}_3$  to produce dititanate  $\text{Ca}_2\text{TiO}_4$ . Destruction of this dititanate phase leads to the formation of equiaxed TiO and the release of  $\text{Ca}^{2+}$  and  $\text{O}^{2-}$  ions into the melt. Finally, TiO is reduced to form a solid solution of oxygen in titanium, Ti–O, concluding the reaction sequence. Metallic titanium is retrieved from the cathode, with oxygen levels as low as 1500 ppm having been reported by technology company Metalysis [16].

Previously, the FFC process routinely made use of high purity  $\text{TiO}_2$  pellet precursors, typically with around 25–30 % porosity [2]. Recent research, however, has now enabled the use of free flowing powder as the feedstock, relinquishing the requirement for a pressed preform [16]. Titanium's ore, rutile ( $\text{TiO}_2$ ), can be obtained from naturally occurring deposits, (hence, known as natural rutile) which is purified via electrostatic and magnetic separation procedures to produce a high purity product [17]. Alternatively,  $\text{TiO}_2$  is

obtained from the more abundant iron-containing ore, ilmenite ( $\text{FeTiO}_3$ ). Rutile created from ilmenite is known as synthetic rutile. A range of methods exist to produce synthetic rutile from ilmenite, such as the Becher, Benelite, Laporte, and Murso processes [17].

It is possible to produce synthetic rutile with varying degrees of purity. Variation in both the type and quantity of impurity present depends on both the source of ilmenite, as well as the method of extraction. Hence, alterations to the extraction process and/or ilmenite source can allow a degree of control over impurity character and content. Typically, synthetic rutile contains both Fe and Al impurities, which are common alloying additions for many commercial titanium alloys, reducing the dependence on costly master alloys further downstream.

Utilisation of synthetic rutile as a feedstock for the FFC process could further reduce the cost of titanium alloy powder production. Taking advantage of a synthetic rutile feedstock firstly minimises costs, as less processing steps are required compared to producing a pure precursor. In 2013, the estimated cost of synthetic rutile was \$1400/t compared with \$3000/t for that of pigment grade  $\text{TiO}_2$  [18]. Secondly, as synthetic rutile naturally contains both alpha and beta stabilisers, titanium alloys can be directly produced. Hence, with further research, a direct route from synthetic rutile to useable, low-cost titanium alloy powder for direct consolidation or near net shaping is a reality, particularly for non-aerospace applications. It is predicted that FFC synthetic rutile derived powder will be competitively priced compared with currently available titanium powders, the cost of which have been recently reported [19].

To take advantage of synthetic rutile feedstock, full characterisation of both the feedstock and the baseline titanium alloy product is necessary. Furthermore, to fully control the process, a thorough understanding of the reduction behaviour throughout electrolysis is required. Hence, this paper presents for the first time, the full characterisation of synthetic rutile at each stage of the reduction process. Partial experiments have allowed an insight into the reaction pathway and behaviour of the synthetic rutile throughout reduction. Previous partial reductions were undertaken using a 99.5 % pure  $\text{TiO}_2$  pressed preform pellets of 25–30 % porosity with an average particle size of 1–2  $\mu\text{m}$ . This set of experiments utilises loose synthetic rutile of particle size 150–212  $\mu\text{m}$  feedstock, which has been reduced and the mechanism compared with the original pure  $\text{TiO}_2$  work [2]. Successful reductions allowed the consolidation of titanium powder derived from synthetic rutile via the spark plasma sintering (SPS) technique.

## Methods and materials

### FFC process reductions

Reduction of synthetic rutile samples (150–212  $\mu\text{m}$ ) supplied by Iluka Resources was achieved at both R&D scale (20 g) and development scale (5 kg). Partial reductions were completed at an R&D scale with powder for consolidation obtained from developmental scale reductions.

The R&D cells consist of a stainless steel retort and lid. Cathode and anode rods are inserted into the lid in addition to a thermocouple. 20 g of each synthetic rutile sample was placed into a steel basket, lined with a stainless steel mesh. A connecting rod was attached to the basket, which screwed into the cathode rod. A carbon anode was screwed into the anode rods. 1.6 kg of dried  $\text{CaCl}_2$  salt contained in a ceramic crucible was placed in the retort before the lid was attached and the retort sealed. Exhaust and water pipes were attached to the lid to allow removal of heat and gases produced. Finally, an argon line is attached to ensure that the reaction occurs under an inert atmosphere. Figure 1 displays the experimental setup utilised for R&D experiments.

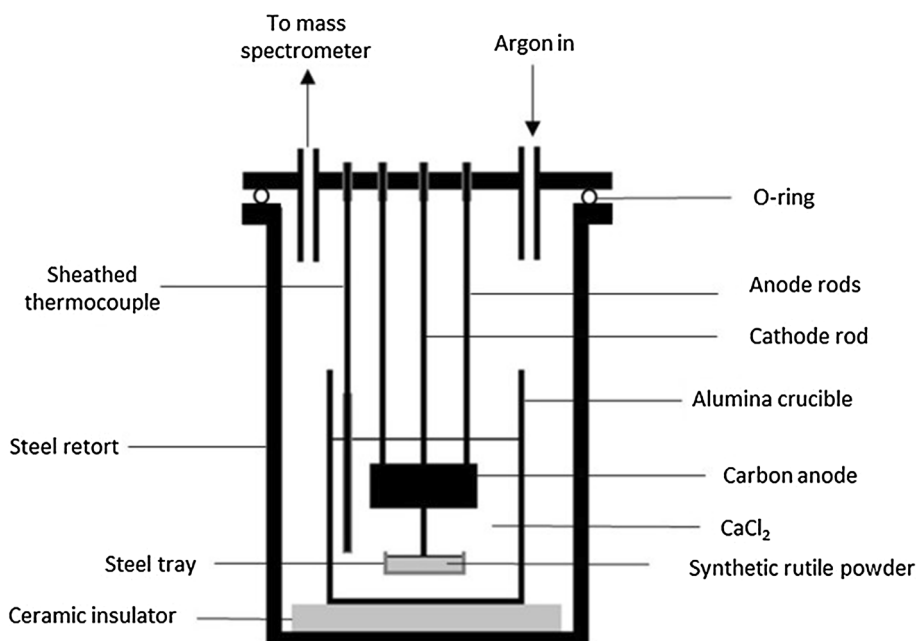
After the cell had been sealed, the temperature was ramped to above 900  $^\circ\text{C}$ . A salt sample was taken by dipping a rod into the molten salt via a viewing port. CaO content of the salt was then determined using an acid–base titration, facilitated by an autotitrator (Mettler Toledo autotitrator T50). Cathode and anodes were then lowered into the molten calcium chloride electrolyte. The depth of the anode and cathode into the salt can be controlled by

measuring the protrusion of the rods in the lid and was kept constant throughout the experiments. Experiments were run at constant current (5A), with an initial current ramp in place to avoid excessive voltages and chlorine formation. The average voltage for completed runs was 3.5 V which was measured at the power supply. The anodic current density for these runs was typically around  $550 \text{ Am}^{-2}$ . Each experiment was timed from the end of the ramp period. Off gases produced by the reaction ( $\text{CO}$  and  $\text{CO}_2$ ) were monitored by mass spectroscopy. Full reductions were ground and washed until the water ran clear to remove any remaining salt. After washing the samples were dried, sieved and weighed.

Partial reductions were interrupted before completion by terminating the applied current and lifting the cathode tray out from the salt into the cooler upper section of the retort. After electrolysis, the partially reduced samples were washed in water and lightly ground before being soaked in hydrochloric acid (1 M). Samples were again washed with water and dried in air at around 80  $^\circ\text{C}$ . Due to the powdered nature of the product and mechanical fragility of some phases, great care was taken to minimise material loss.

Once clean and dry, samples were analysed using X-ray diffraction (XRD) techniques outlined below, followed by microstructural studies, with the exception of the 2 h partial, in which microstructure studies took place from a repeated non ground sample due to the mechanical fragility of the  $\text{Ca}_2\text{TiO}_4$  needles. Each of the time intervals was completed at least twice.

**Fig. 1** Experimental setup of an R&D reduction cell



## X-ray diffraction (XRD) analysis

Samples were ground before XRD analysis using a Bruker D2 phaser and Cu-K $\alpha$  radiation. Samples were scanned throughout the range of 10–80°. Phase analysis was completed using the International Centre for Diffraction Data (ICDD) database, with the following powder diffraction file (PDF) cards being utilised: Ti<sub>2</sub>O<sub>3</sub> (01-074-0324), Ti<sub>3</sub>O<sub>5</sub> (04-008-8183), CaTiO<sub>3</sub> (04-012-0563), TiO (04-004-9041), CaTi<sub>2</sub>O<sub>4</sub> (04-010-0703), Ti<sub>2</sub>O (04-005-4357),  $\alpha$ -Ti (04-008-4973).

## Morphology

Following mounting in conductive Bakelite, samples were subjected to grinding and polishing using silicon carbide papers, diamond paste and Struers OP-S polishing suspension. Scanning electron microscopy (SEM) images were taken using a JEOL-JSM6490LV using an acceleration voltage of 20 keV.

## Chemical analysis

Oxygen content was measured using an Eltra ON-900. X-ray fluorescence (XRF) data were collected using a Phillips PW 2404. X-ray energy-dispersive spectroscopy (X-EDS) was performed using INCA software on the aforementioned scanning electron microscope. Finally, inductively coupled plasma-mass spectroscopy (ICP-MS) analysis was performed by Metalysis using a Thermo X series 2.

## Consolidation

Consolidation was achieved via a spark plasma sintering technique using a FCT system e GmbH spark plasma sintering furnace-type HP D 25. 17 g of powder was placed into a 20-mm-diameter graphite ring mould with two pistons, lined with graphite paper. A carbon felt jacket was added to prevent heat loss [20]. Once loaded into the SPS machine, the sample underwent a predetermined sintering cycle, involving a ramp rate of 100 °C/min, an applied force of 15 kN and a dwell time of 30 min at 1200 °C. Any remaining graphite paper was removed by grit blasting to yield a 10 mm × 20 mm consolidated synthetic rutile pellet.

## Results and discussion

Due to the nature of the experimentation, microstructural studies could not be completed in situ. Hence, further crystallographic transformations are possible during the

cooling of the cell [15]. For example, the observed Ti<sub>2</sub>O phase occurring at 4 h of reduction, would not form in situ as this phase is a product of the Ti–O phase cooling to room temperature [4]. Other changes are possible such as the growth of CaTi<sub>2</sub>O<sub>4</sub> needles during the cooling down of the sample.

## Characterisation of synthetic rutile

The angular and porous morphology of synthetic rutile feedstock is shown in Fig. 2. This porosity is inherent from its extraction route, the Becher process, which leaches out iron from ilmenite in an ‘accelerated rusting’ procedure [17, 21]. Due to this extraction process, the synthetic rutile produced tends to be porous and shows a small level of chemical heterogeneity.

The synthetic rutile used for this particular study possesses a range of particle shapes and sizes. Likewise, the pores contained within the rutile are equally as heterogeneous with a hierarchical range of pore sizes, shapes, and distributions. In some extremes, hollow particles can be observed as shown in Fig. 2c. Remnant iron not removed from the Becher process can be identified as small white dots under Z contrast backscatter imaging. Chemistry of the synthetic rutile (150–212  $\mu$ m) was also analysed via XRF spectroscopy to reveal a composition of around 4 % beta stabilising transition elements and less than 1 % aluminium.

## Partial reductions of synthetic rutile

As discussed earlier, due to the high temperature, inert atmosphere and current required, in situ spectroscopy techniques were deemed impractical for microstructural studies. Instead, the reaction was stopped at timed intervals to gain an insight into the behaviour of synthetic rutile at various points throughout the reaction pathway. Samples were taken at 0.5, 1, 2, 4 and 8 h, with full reduction occurring at 16 h. Oxygen analysis, XRD, SEM and XRF techniques were used to characterise the partially reduced samples.

Samples reduced for less than 8 h were generally dark in colour, with the exception of 30 min reductions exhibiting a shade of brown–orange. However, the sample reverted back to black after acid washing overnight. It is thought this colour arises from iron precipitating out of solid solution. Both 4 and 8 h samples required two overnight acid washes to remove the high level of CaO and CaCO<sub>3</sub> remaining within the sample.

Following the addition of acid to the sample during the washing procedure, some partially reduced samples exhibited a layer of floating scum on top of the aqueous phase. Only small samples of the scum were obtained and

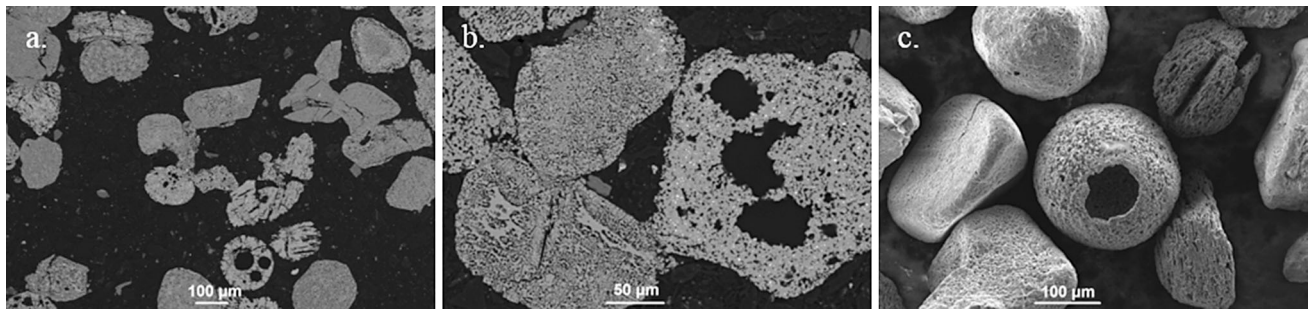


**Fig. 2** Synthetic rutile feedstock. **a** and **b** backscattered electron images of synthetic rutile. **c** secondary electron image of synthetic rutile feedstock

were analysed via X-EDS. After 1 h of reduction, a gold scum formed, containing Ca, Cl, O, Ti and Fe, which gave rise to its colour. After 4 and 8 h, a silver scum formed which consisted mainly of C, O and Ca and occasionally small amounts of titanium. It is likely that the scum formed contains a combination of free C and  $\text{CaCO}_3$ .  $\text{CaCO}_3$  has been observed previously, and more detailed explanations can be found [8].

Each of the partial samples were subjected to XRD analysis, with a good reproducibility of the phases being found. Detection of phases was restricted by the limited sensitivity of the XRD technique, with only major phases being detected ( $>5\%$ ). Furthermore, the complex Ti–O system contains many suboxides, producing similar crystallographic peaks, (e.g.  $\text{Ti}_3\text{O}$  and  $\text{Ti}_6\text{O}$ ) which can make identification of some phases strenuous [2]. Figure 3 shows the XRD patterns produced from the reductions.

After 30 min of electrodeoxidation, XRD reveals major phases of  $\text{Ti}_3\text{O}_5$ ,  $\text{Ti}_2\text{O}_3$  and  $\text{CaTiO}_3$  (Fig. 3a). Requiring minimal atomic reconstruction, these phases have previously been observed by Schwandt et al., following the reaction pathway via Eqs. 2 and 3 [2, 3]. This work [2, 3] has also deduced that the initial step of the reduction is the incorporation of Ca into the cathode, which is highlighted by the increase in Ca content and decrease in Ti content at 30 min of polarisation, as illustrated by Fig. 4. Figure 4 also displays the oxygen content throughout the reduction process. Note, at high levels of oxygen these numbers are indicative values only as the instrument is calibrated for low levels of oxygen content.

The brown orange colour residue observed after 30 min of reduction following removal of the salt is postulated to be due to the presence of iron, which had precipitated out of solid solution. Once washed in HCl, the iron was removed, reverting to a black powder with a substantially reduced iron content. Iron is a beta stabiliser and rapidly diffuses within titanium [22]. Furthermore, from a thermodynamic consideration, iron oxide reduces more readily than titania via the FFC process. Hence, as iron has

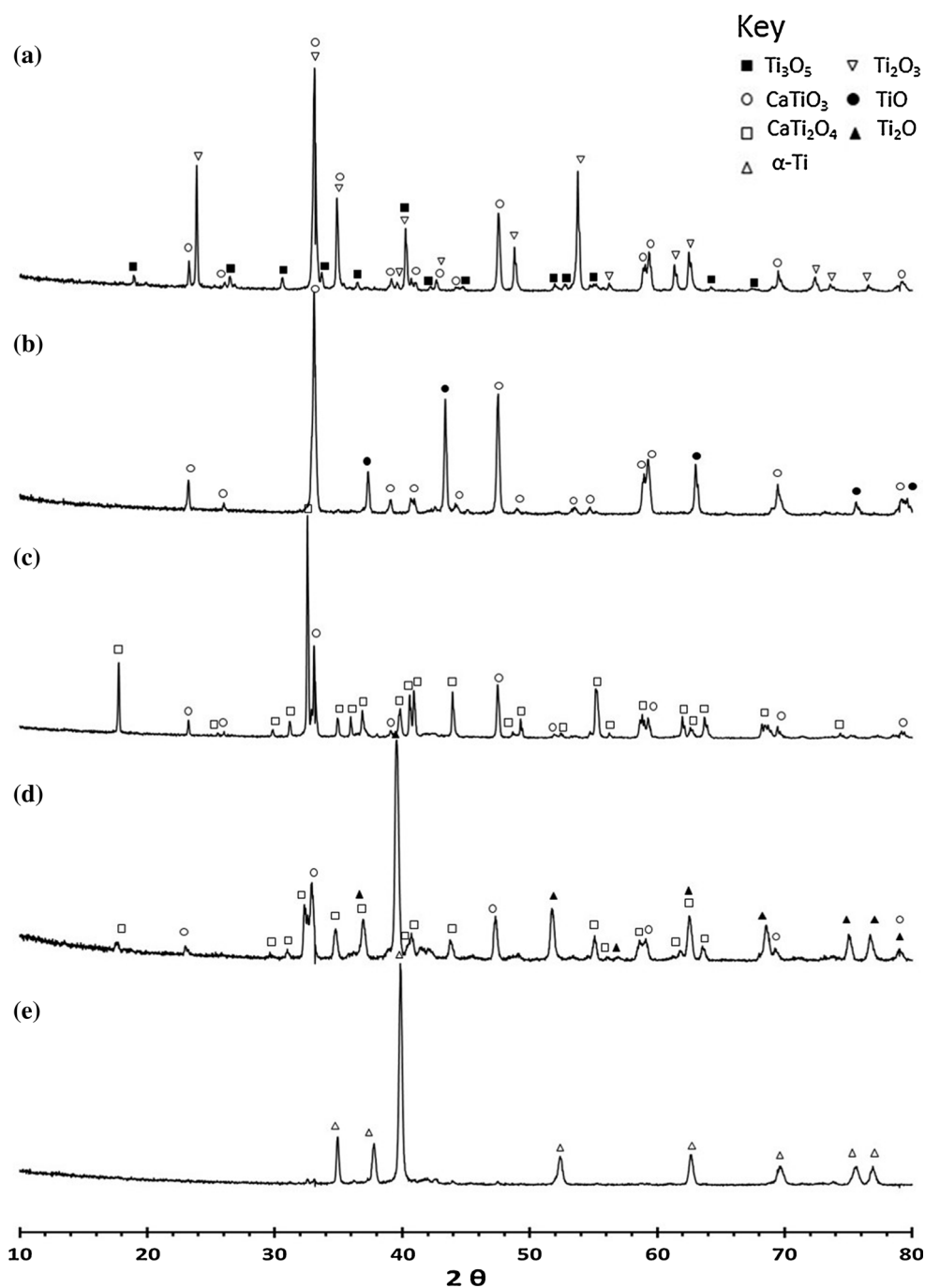
precipitated out after 30 min of polarisation, evidence from this work suggests that iron has reduced within this time frame and has migrated out of solid solution.

Morphology of the particles after 30 min of reduction shows two distinct phases. Larger solid appearing areas have been analysed to reveal calcium, titanium and oxygen content. Therefore, these areas have been identified via X-EDS analysis, as the  $\text{CaTiO}_3$  phase, shown in Fig. 5b. Smaller pieces with a more fragmented appearance show a decreased presence of calcium and consist mainly of titanium and oxygen. Therefore, these areas have been identified as a combination of the titanium suboxide phases.

After reduction of synthetic rutile for 1 h, the iron has reduced, shown in Fig. 5e as the heavy, bright white phase. It is believed this iron-rich phase has diffusion bonded to the surrounding suboxide phase. Identification of the phase using X-EDS analysis was limited due to the large interaction volume with respect to the low volume fraction of the iron-containing phase. The stoichiometry of this intermetallic phase shows a wt% ratio of roughly 30:70 (Ti:Fe). Thus, it can be deduced that the intermetallic  $\text{TiFe}_2$  phase has formed.  $\text{TiFe}_2$  was not detected by XRD due to its low concentrations. Only two major phases consisting of cubic TiO and  $\text{CaTiO}_3$  were detected by XRD at this point in the reduction (Fig. 3b). Again, the formation of the TiO phase is in agreement with the reaction mechanism outlined earlier by Schwandt et al., as shown in Eq. 4 [2]. At this stage in the reduction, a kinetic barrier is expected as the lattice shape shifts from edge sharing  $\text{Ti}_2\text{O}_3$  octahedra, to cubic titanium oxide [3]. Figure 5d–f depicts the morphology observed at this stage in the process, illustrating the formation of agglomerate particles consisting of TiO and  $\text{CaTiO}_3$ .

Following the formation of TiO, the reaction proceeds to the formation of calcium dititanate at around 2 h of polarisation. This stage features the largest reconstructive transformation throughout the reduction, with the formation of the lath-shaped acicular  $\text{CaTi}_2\text{O}_4$  (Eq. 5). Due to the low mechanical stability of the dititanate phase, a further

**Fig. 3** X-ray diffraction spectrum of partially reduced samples of synthetic rutile at various timed intervals **a** 0.5 h showing  $\text{Ti}_3\text{O}_5$ ,  $\text{Ti}_2\text{O}_3$  and  $\text{CaTiO}_3$  **b** 1 h showing  $\text{TiO}$  and  $\text{CaTiO}_3$  **c** 2 h showing  $\text{CaTiO}_3$  and  $\text{CaTi}_2\text{O}_4$  **d** 4 h showing  $\text{Ti}_2\text{O}$ ,  $\text{CaTiO}_3$  and  $\text{CaTi}_2\text{O}_4$ . **e** 8 h showing  $\alpha\text{-Ti}$



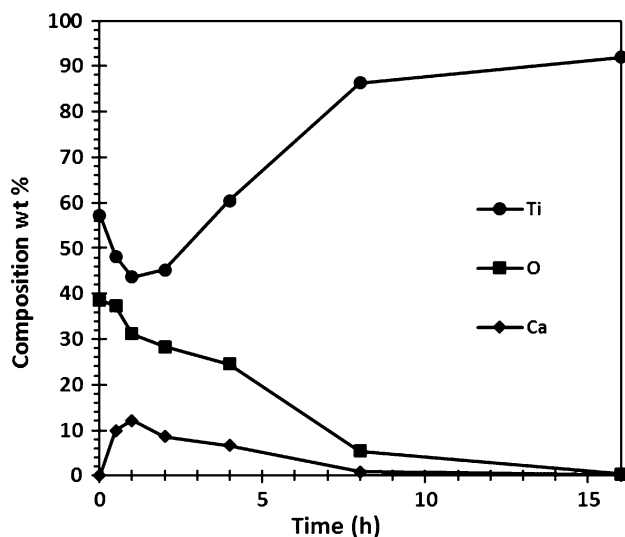
repeated partial reduction halted at 2 h was performed in order to observe the needles before the sample was ground for XRD analysis. Backscattered electron images show clearly the presence of both titanates; the needle-like  $\text{CaTi}_2\text{O}_4$  and the more faceted  $\text{CaTiO}_3$  are shown in Fig. 6b and c. Formation of  $\text{CaTi}_2\text{O}_4$  has previously been reported to grow in a “star burst” manner, which was also observed and shown in Fig. 6c. This star burst pattern has previously been explained as a result of limited nucleation and fast

anisotropic growth at low angles of misorientation [3]. Figure 6c also highlights an enlarged image of a faceted  $\text{CaTiO}_3$  particle.

The presence of the iron as discrete  $\text{TiFe}_2$  particles is still clear at this point in the reduction. However, occasionally, a thin layer of a less bright phase coats the  $\text{TiFe}_2$  phase. It is thought that as the reaction proceeds, the iron within the  $\text{TiFe}_2$  particles begins to diffuse into surrounding suboxides to form a thin layer of  $\text{TiFe}$  around the  $\text{TiFe}_2$

core. Formation of the TiFe phase is discussed in more detail at 4 h of reduction.

At 4 h, both titanates are still present, alongside newly formed  $\text{Ti}_2\text{O}$  (Fig. 3d). Note, an unidentified peak is observed in the XRD pattern at  $42^\circ$ , which persists at 8 h of reduction. It has previously been reported that the  $\text{Ti}_2\text{O}$  phase is a product of the cooling of the Ti–O phase [4], which can be observed in the Ti–O phase diagram shown in



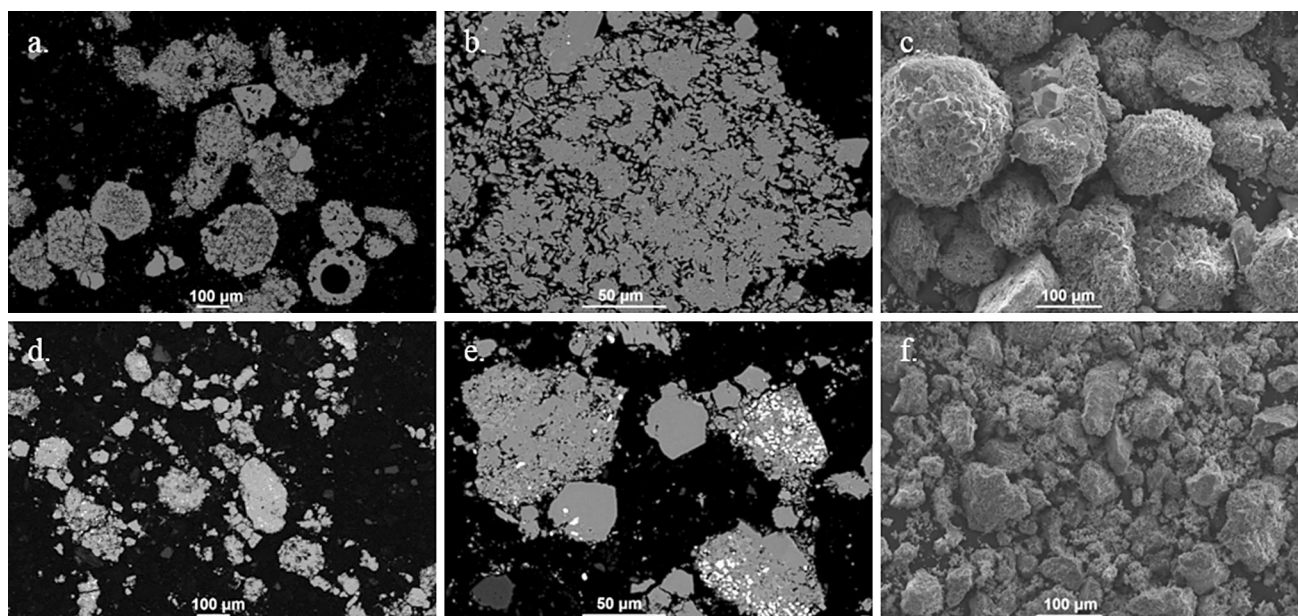
**Fig. 4** Chemical composition in wt% of titanium, calcium, and oxygen throughout the reduction of synthetic rutile as measured by XRF analysis. Calcium levels at 0 and 16 h measured by ICP-MS due to low contents

Fig. 7. During this stage of the reduction, destruction of the ditanate produces oxide ions alongside  $\text{Ca}^{2+}$ , resulting in the high content of CaO throughout the sample (Eq. 6). Hence, extra acid washing was required at this stage to remove the calcium oxide. Morphology of the particles at this point is somewhat mixed, with some particles showing little resemblance to the initial spherical style particle they are evolved from. Secondary electron images reveal nodular growth of a globular nature.

Additionally, at 4 h of reduction, bright, highly concentrated areas of iron begin to noticeably reduce in size and intensity. Areas of high iron concentration now display two clear phases, easily identifiable due to the difference in contrast. Porosity around the phase edges also affirm the formation of a second iron-containing phase. Again, identification of this second iron-containing phase (TiFe) using X-EDS analysis was limited due to the large interaction volume with respect to the low volume fraction of the phase.

However, it appears the core  $\text{TiFe}_2$  remains, with the second coating phase containing a lower concentration of iron. From the Ti–Fe–O phase diagram (Fig. 8), the limited X-EDS data available and SEM images, it is plausible that the TiFe phase has formed a layer surrounding the  $\text{TiFe}_2$  core.

After just 8 h,  $\alpha$ -titanium is identified as the major phase by XRD analysis (Fig. 3e). Note,  $\alpha$ -Ti can contain approximately up to 15 wt% oxygen [26] (Fig. 7) and as shown by Fig. 4, at 8 h this sample contains around 5 wt% oxygen. Other phases may be present, as shown by the



**Fig. 5** Partially reduced synthetic rutile. **a** and **b** show backscattered electron images of partially reduced synthetic rutile morphology after 0.5 h and **d** and **e** after 1 h. Figures **c** and **f** represent secondary electron images after 0.5 and 1 h of reduction, respectively

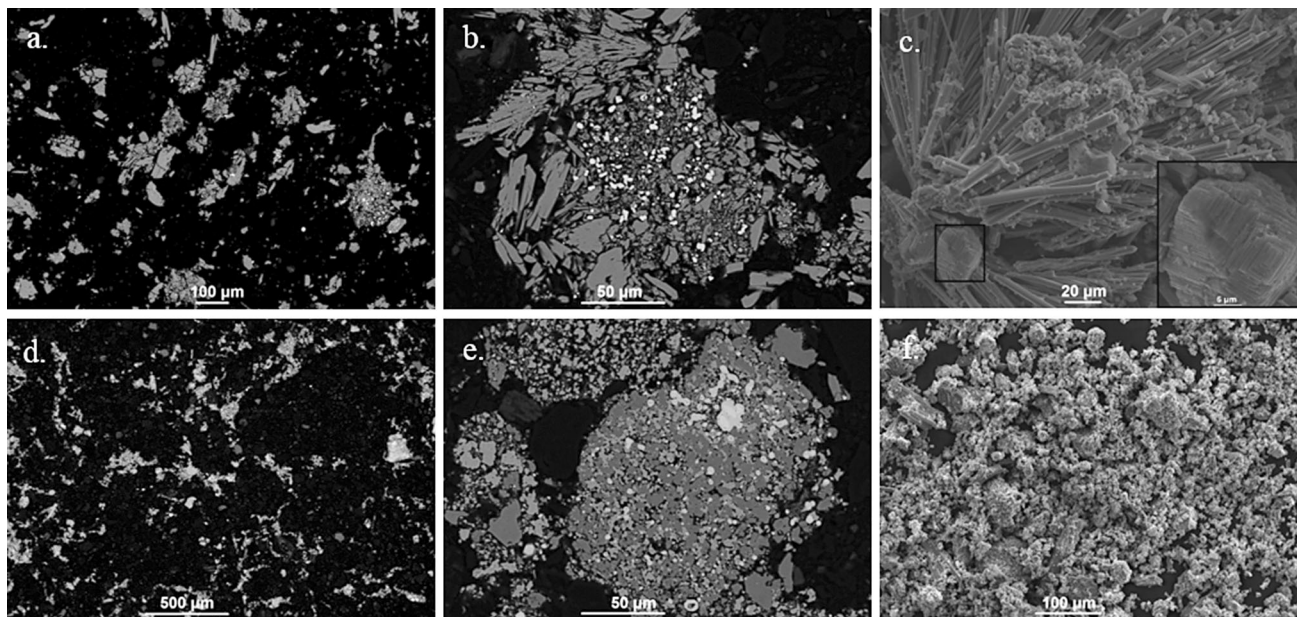
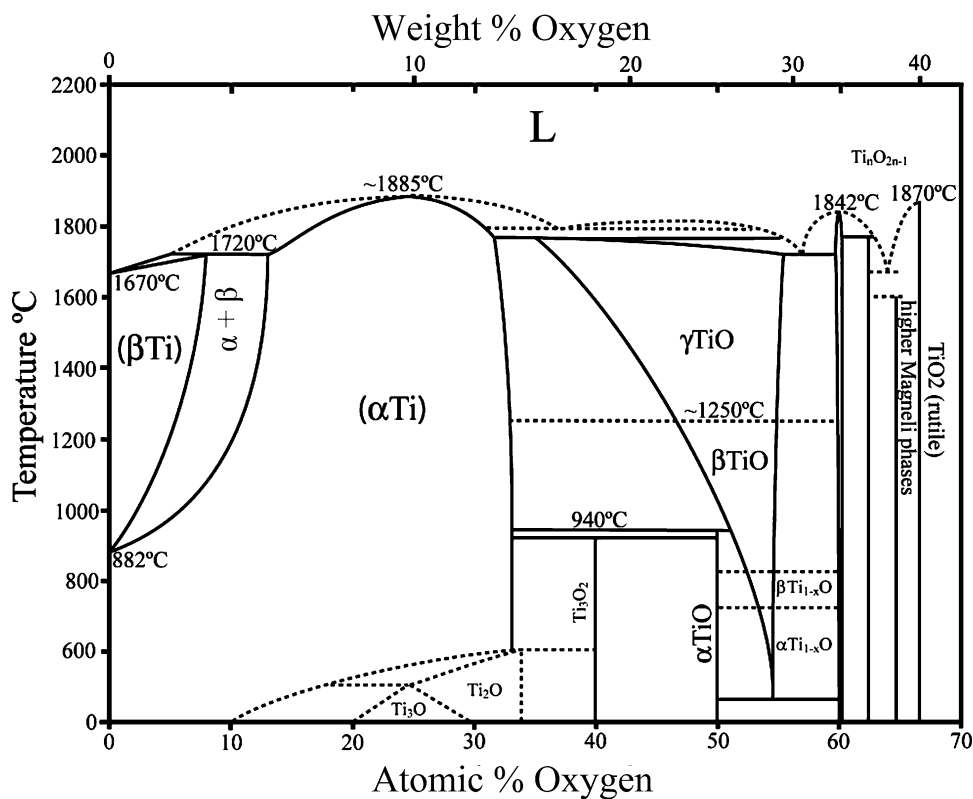


**Fig. 6** Partially reduced synthetic rutile. **a** and **b** show backscattered electron images of partially reduced synthetic rutile after 2 h and **d** and **e** after 4 h. Figures **c** and **f** represent secondary electron images after 2 and 4 h of reduction, respectively

**Fig. 7** Binary phase diagram of Ti–O [23]



presence of peaks at 32.5°, 36°, and 42° mentioned earlier, which were unable to be identified. An interconnected porous system is beginning to take shape, shown in Fig. 9b which exhibits two separate phases, identified as alpha and beta titanium. At this point in the reduction, the final morphology begins to evolve, which is comparable to that

of the final product shown in Fig. 9d and f. It is imperative to note at this stage in the reduction, no intermetallics or areas of excessive iron content can be found; the iron has fully dispersed throughout each particle.

Completion of the reduction occurs at 16 h, giving a final oxygen content of approximately 4000 ppm. The



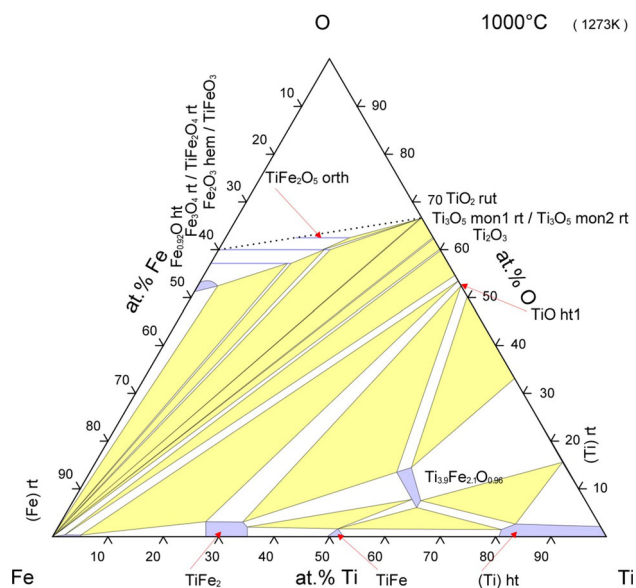


**Fig. 8** Tertiary Phase diagram of Ti–Fe–O [24, 25]

particles now have a much more sintered morphology. Again alpha and beta phases can be identified in the backscattered images (Fig. 9e). The predominant morphology, a fine scale alpha beta structure (Fig. 9e), was found alongside a more lamellar structure which could be a product of slight local particle to particle chemical variation observed in the feedstock. Chemical composition of the reduced synthetic rutile was found to contain alpha stabilising aluminium, as well as 4.4 % of beta stabilising transition elements.

Overall it appears as though the reaction pathway is in agreement with that previously reported by Schwandt et al. [2]; however, there are some significant differences in this system warranting further discussion. A new major feature is apparent in the formation and subsequent reduction of iron intermetallic phases. Initially iron present within the synthetic rutile is reduced to metallic Fe after 30 min of reduction. Following the reduction of iron oxide is the formation of the intermetallic  $\text{TiFe}_2$  as compact discrete particles, easily identifiable as the bright phase in backscattered images (Fig. 10a). As the reduction progresses the iron diffuses into the surrounding titanium suboxides, giving rise to  $\text{TiFe}$ . A coexistence of these phases can be seen in the titanium–iron phase diagram (Fig. 8). Both intermetallic phases are observed in Fig. 10b and c, with the bright core of the iron-based particle consisting of  $\text{TiFe}_2$  and the outside exhibiting the less bright  $\text{TiFe}$  phase. Further dispersion of the concentrated iron occurs with further diffusion of iron into surrounding suboxides. A solid solution of iron in titanium begins to appear with high contents of iron (up to 60Ti:40Fe) confirming its diffusion into the surrounding titanium (Fig. 10c).

High local concentrations of  $\beta$  stabilising iron leads to a widening of the  $\alpha + \beta$  and  $\beta$  phase fields at the expense of the  $\alpha$  phase field (Fig. 7). Widening of these phase fields allows a faster reduction within these areas due to the presence of beta titanium, in which oxygen diffuses at least two orders of magnitude faster than within alpha titanium. Occasionally, rare particles of high oxygen titanium metal are observed at 4 h (Fig. 10d). The formation of titanium

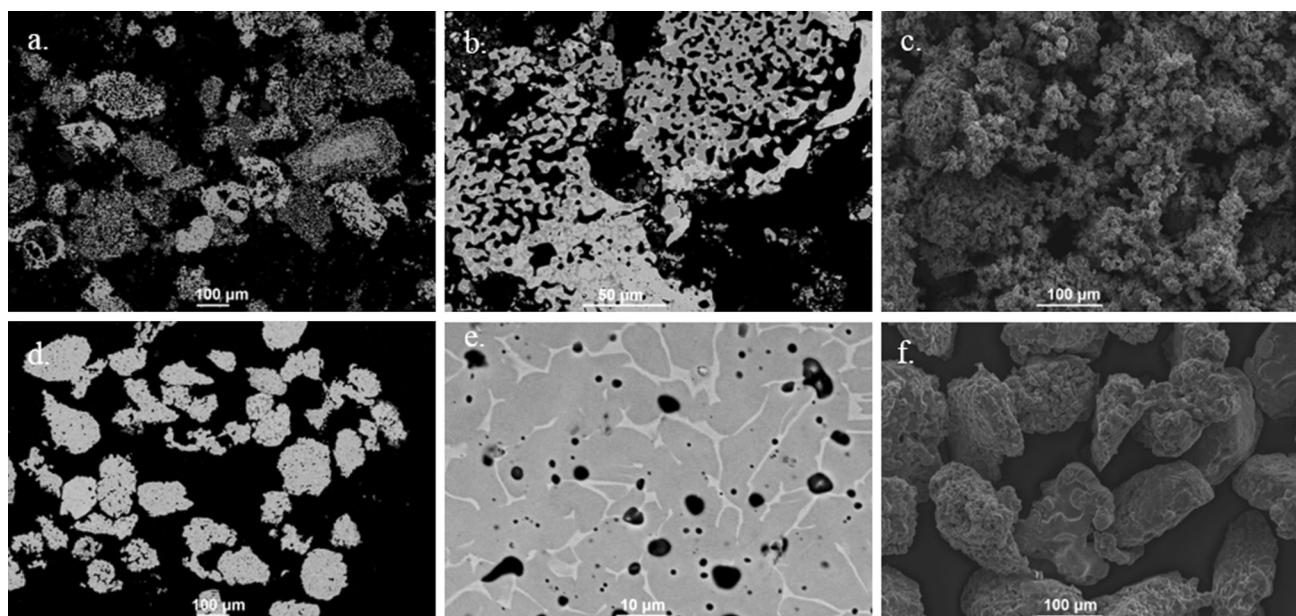


**Fig. 9** Partially and fully reduced synthetic rutile. **a** and **b** are backscattered electron images of partially reduced synthetic rutile after 8 h and **d** and **e** after 16 h (completion). Figures **c** and **f** represent secondary electron images after 8 and 16 h of reduction, respectively

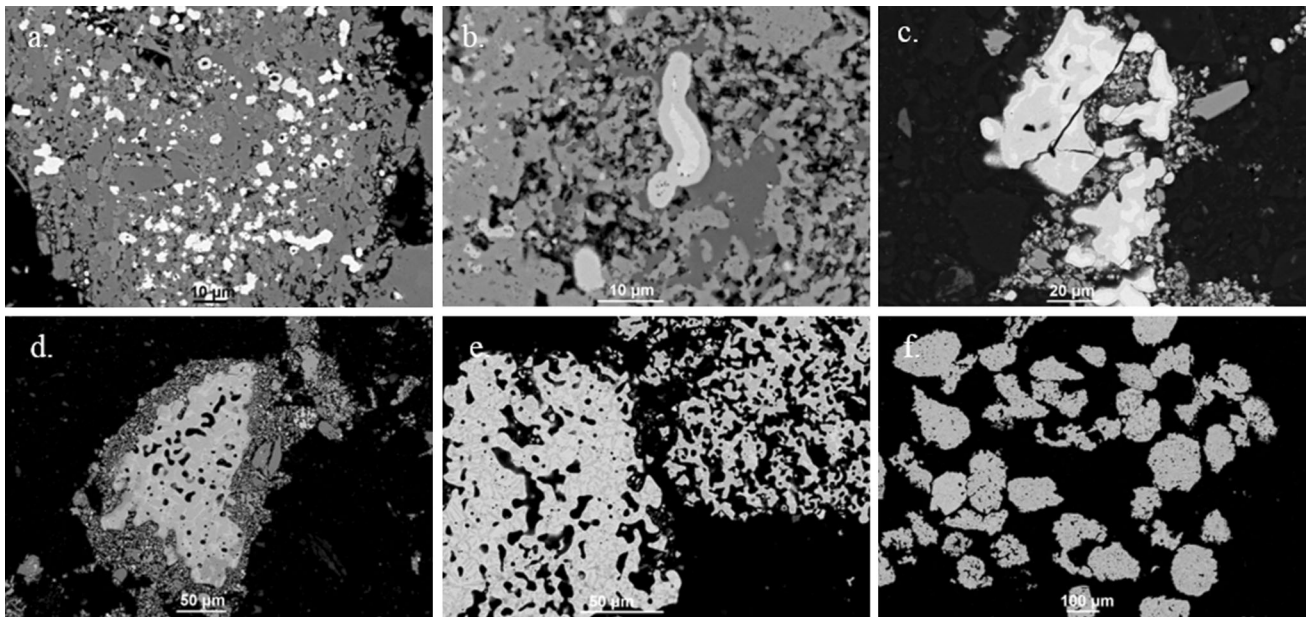


**Fig. 10** Backscattered electron images of a partial reduced synthetic rutile samples. **a** After 1 h of reduction, highlighting the bright  $\text{TiFe}_2$  phase. **b**, **c** and **d** After 4 h of reduction with **b** Showing a  $\text{TiFe}_2$  core surrounded by a  $\text{TiFe}$  layer. **c** Illustrates a bright  $\text{TiFe}_2$  surrounded by titanium with iron content ranging from 40 to 50 %. **d** Rare particle showing the first formation of titanium metal consisting mostly of

beta titanium, surrounded by titanium suboxides and  $\text{CaTiO}_3$ . **e** Particles after 8 h of reduction, left particle is beta rich and slightly more sintered whereas the right particle is alpha dominant and is less sintered. **f** Fully reduced material showing beta phase is well dispersed within final particles

this early on in the reduction is likely due to the particles containing high quantities of iron, allowing the formation of the high oxygen beta phase and faster diffusion process. Particles containing reduced titanium at 4 h of reduction often contained significant quantities of the beta phase.

Iron continues to disperse throughout the reducing titanium metal and after 8 h of reduction, no observable intermetallic compounds are found. Iron is found to be evenly dispersed throughout the beta phase of the resulting reduced particle. However, an observation was made that particles containing higher proportions of the beta phase (appearing lighter under backscatter imaging) were clearly more sintered than particles that were alpha dominant as shown in Fig. 10e. This enhanced sintering is due to the faster diffusion rate of oxygen within beta titanium and as such, slightly faster reduction. However, at the end of reduction, most particles are sintered to a similar extent with iron fully dispersed throughout the beta phase of each particle (Fig. 10f).

### Consolidation and forging

Due to the success of the R&D scale reductions (20 g), the reduction of synthetic rutile was scaled up to developmental scale (5 kg). A slightly different feedstock was chosen to reduce at development scale with a transition element concentration of 3.7 % and aluminium content of

less than 1 %. At developmental scale reduced synthetic rutile samples have produced oxygen contents as low as around 2000 ppm. A sample of 3500 ppm oxygen containing around 3.4 % transitional beta stabilising elements and less than 1 % aluminium reduced synthetic rutile was consolidated using a spark plasma sintering technique. Spark plasma sintering is a consolidation technique in which powder is pressed together under a uni-axial pressure combined with elevated temperatures and an applied current [20, 27]. Figure 11 displays the microstructure achieved after consolidation as analysed by SEM.

Despite originating from a porous synthetic rutile feedstock, containing slight chemical inhomogeneity between particles, following reduction and consolidation via spark plasma sintering, a fine  $\alpha + \beta$  homogenous microstructure has emerged. Coarse pro-eutectoid acicular alpha regions dominate the microstructure, with a much finer eutectic  $\alpha + \beta$  phase featured between the larger laths. Porosity can be observed within the sample, and has been measured to give a density value of approx. 98.6 %. Although this value is lower than the >99 % commonly achieved by commercial titanium alloys [20], this porosity was obtained using standardised, non-optimised conditions. Furthermore, SPS or field-assisted sintering technology (FAST) is envisaged to be an intermediate step and a precursor to hot forging processes where further microstructure refinement and removal of residual porosity will be achieved.

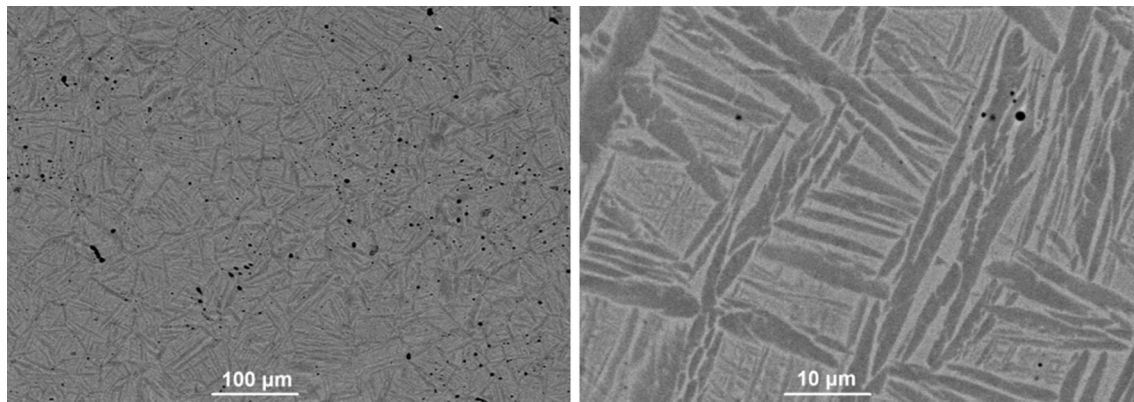


**Fig. 11** Backscattered image of consolidated reduced synthetic rutile of oxygen content ca. 3500 ppm

## Conclusion and future work

Partial reductions of synthetic rutile exploiting XRD, SEM and oxygen analysis revealed no major deviations from the reaction pathway previously outlined by Schwandt et al. [2], despite the presence of remnant elements from the Becher process. However, the monoclinic TiO phase was not found. Additionally, due to the presence of iron, new features of the reduction were noted, with particular emphasis on the reduction pathway of iron and the formation of intermetallics TiFe<sub>2</sub> and TiFe. These intermetallics are deconstructed and the iron is fully dispersed throughout the reduced alloy product. However, slight inhomogeneity remains on a local level with some particles displaying a richer beta microstructure.

As previous work reported by Schwandt et al. [4, 5] has shown that the reduction mechanism may be altered if conditions are changed such as CaO content, ramp rate and density of the preform, further work may be required to detect if the reduction mechanism of synthetic rutile responds in the same way. Further, due to the powdered nature of the feedstock, it was more difficult to establish if direct reduction as mentioned in previous work is occurring, hence future work may require the use of preform pellet to determine this.

Consolidation of synthetic rutile reduced titanium alloy powder has been successfully achieved, resulting in a fine  $\alpha + \beta$  microstructure of 98.6 % porosity using non-optimised sintering conditions. Further work will consist of optimising downstream processing as well as improving the mechanical properties of titanium alloy powders produced from synthetic rutile feedstock.

Overall the reduction of synthetic rutile has produced promising results. These results show that with further development, the FFC process is capable of producing low-cost titanium alloys produced directly from synthetic rutile. Further, the presence of beta stabilising elements appears to

facilitate a faster and more efficient solid-state reduction [8]. Many of these beta stabilisers are prone to chemical segregation when produced using conventional melt processing techniques (such as beta flecks). Using a combination of Metalysis FFC powder and low-cost powder consolidation methods, a pathway is established that is entirely performed in the solid-state eliminating such segregation issues.

Current metastable  $\beta$  alloys such as Ti–10V–2Fe–3Al and Ti–5Al–5V–5Mo–3Cr are currently still hindered by their tendency to segregate during vacuum arc remelting, as well as high costs of downstream thermomechanical processing to homogenise chemistry and refine microstructure. These alloys have been notorious to displace, despite the production of alloys with improved properties, due to the high cost of qualification [28]. However, with further research, these alloys may one day be overhauled by beta stabilised alloys produced directly from synthetic rutile, allowing the modernisation of current metastable beta alloys targeted towards non-aerospace sectors.

**Acknowledgements** The authors gratefully acknowledge the financial support of the Engineering and Physical Sciences Research Council UK (EPSRC) through the Centre for Doctoral Training in Advanced Metallic Systems and technology company, Metalysis. The authors would like to thank Prof. Panos Tsakiroopoulos for useful discussions, Nick Weston for his SPS guidance and Dr. Nik Reeves-McLaren for his assistance with XRD experimentation. Thanks also goes to the Metalysis technology team (Nader Khan, Greg Doughty, Joseph Campion, Terri Ellis, Matt Piper & Ruth Graham), analytical team (Dan Kitson, Basharat Ali & Becky Micklethwaite) and operations team.

**Funding** Funding for this research was provided by the Engineering and Physical Sciences Research Council and Metalysis.

**Compliance with ethical standards**

**Conflict of interest** Author Ian Mellor has a vested interest in the Metalysis Company. No other conflicts of interest.

**Open Access** This article is distributed under the terms of the Creative Commons Attribution 4.0 International License (<http://creativecommons.org/licenses/by/4.0/>), which permits unrestricted use, distribution, and reproduction in any medium, provided you give appropriate credit to the original author(s) and the source, provide a link to the Creative Commons license, and indicate if changes were made.

## References

- Chen GZ, Fray DJ, Farthing TW (2000) Direct electrochemical reduction of titanium dioxide to titanium in molten calcium chloride. *Nature* 407:361–364
- Schwandt C, Fray DJ (2005) Determination of the kinetic pathway in the electrochemical reduction of titanium dioxide in molten calcium chloride. *Electrochim Acta* 51(1):66–76
- Alexander DTL, Schwandt C, Fray DJ (2006) Microstructural kinetics of phase transformations during electrochemical reduction of titanium dioxide in molten calcium chloride. *Acta Mater* 54:2933–2944
- Schwandt C, Alexander DTL, Fray DJ (2009) The electroreduction of porous titanium dioxide precursors in molten calcium chloride under cathodic potential control. *Electrochim Acta* 54:3819–3829
- Alexander DTL, Schwandt C, Fray DJ (2011) The electroreduction of dense titanium dioxide precursors in molten calcium chloride giving a new reaction pathway. *Electrochim Acta* 56:3286–3295
- Barnett R, Kilby KT, Fray DJ (2009) Reduction of tantalum pentoxide using graphite and tin-oxide-based anodes via the FFC-Cambridge process. *Metal Mater Trans B* 40B:150–157
- Bhagat R (2008) The electrochemical formation of titanium alloys via the FFC Cambridge process, Imperial College London, PhD thesis
- Bhagat R, Jackson M, Inman D, Dashwood R (2008) The production of Ti-Mo alloys from mixed oxide precursors via the FFC Cambridge process. *J Electrochem Soc* 155:E63–E69
- Chen G, Fray DJ (2006) A morphological study of the FFC chromium. *Trans Inst Min Metall C* 115:49–54
- Dring K, Bhagat R, Jackson M, Dashwood RJ, Inman D (2006) Direct electrochemical production of Ti-10W alloys from mixed alloys precursors. *J Alloy Compd* 419:103–109
- Jackson BK, Jackson M, Dye D, Inman D, Dashwood RJ (2008) Production of NiTi via the FFC Cambridge process. *J Electrochem Soc* 155:E171–E177
- Dring K, Dashwood R, Inman D (2005) Voltammetry of titanium dioxide in molten calcium chloride at 900 C. *J Electrochem Soc* 152(3):E104–E113
- Jiao S, Fray DJ (2010) Development of an inert anode for electro-winning in calcium chloride-calcium oxide melts. *Metal Mater Trans B* 41B:74–79
- Jackson M, Dring K (2006) A review of advances in processing and metallurgy of titanium alloys. *Mater Sci Technol* 22:881–887
- Bhagat R, Dye D, Raghunathan SL, Talling RJ, Inman D, Jackson BK, Rao KK, Dashwood RJ (2010) In situ synchrotron diffraction of the electrochemical reduction pathway of TiO<sub>2</sub>. *Acta Mater* 58(15):5057–5062
- Mellor I, Grainger L, Rao K, Deane J, Conti M, Doughty G, Vaughan D (2015) Titanium powder production via the Metalysis process, in *Titanium powder metallurgy*. Butterworth-Heinemann, Oxford, pp 51–67
- Zhang W, Zhu Z, Cheng CY (2011) A literature review of titanium metallurgical processes. *Hydrometallurgy* 108:177–188
- van Vuuren DS (2015) Direct titanium powder production by metallothermic processes, in *titanium powder metallurgy*. Butterworth-Heinemann, Oxford, pp 69–93
- Froes FH (2013) Titanium powder metallurgy: developments and opportunities in a sector poised for growth. *Powder Metall Rev* 2(4):29–43
- Weston NS, Derguti F, Tudball A, Jackson M (2015) Spark plasma sintering of commercial and development titanium alloy powders. *J Mater Sci* 50(14):4860–4878. doi:10.1007/s10853-015-9029-6
- Iluka Resources (2012) Iluka's synthetic rutile production. <http://www.iluka.com/docs/mineral-sands-briefing-papers/iluka's-synthetic-rutile-production-june-2012>. Accessed 1 Oct 2015
- Nakajim H, Koiwa M (1991) Diffusion in titanium. *ISIJ Int* 31(8):757–766
- Murray JA, Wriedt HA (1994) In: Boyer RR, Welsch G, Collings EW (eds), *Materials properties handbook: titanium alloys*. Ohio: ASM International
- Raghavan V (1989) The Fe-O-Ti (iron-oxygen-titanium) system, phase diagrams ternary iron alloys. *Indian Inst Met* 5:300–325
- Raghavan V (2006) Ti-O-Fe phase diagram. *ASM alloy phase diagrams database*, Villars P, editor-in-chief, Okamoto H, Cenzual K (eds). <http://www1.asminternational.org/AsmEnterprise/APD>. Materials Park
- Molchanova EL (1965) Phase diagrams of titanium alloys. *Isreal Program for Scientific Translations*, Jerusalem
- Munir ZA, Anselmi-Tamburini U, Ohyanagi M (2006) The effect of electric field and pressure on the synthesis and consolidation of materials: a review of the spark plasma sintering method. *J Mater Sci* 41(3):763–777. doi:10.1007/s10853-006-6555-2
- Cotton JD, Briggs RD, Boyer RR, Tamirisakandala S, Russo P, Shchetnikov N, Fanning JC (2015) State of the art in beta titanium alloys for airframe applications. *JOM* 67(6):1281–1303